Flexible Multi-Turn Multi-Gap Coaxial RF Coils: Design Concept and Implementation for Magnetic Resonance Imaging at 3 and 7 Tesla

Lena Nohava, *Associate Member, IEEE*, Raphaela Czerny, Sigrun Roat, Michael Obermann, Andre Kuehne, Roberta Frass-Kriegl, Jacques Felblinger, *Member, IEEE*, Jean-Christophe Ginefri, and Elmar Laistler

***Abstract*— Magnetic resonance has become a backbone of medical imaging but suffers from inherently low sensitivity. This can be alleviated by improved radio frequency (RF) coils. Multi-turn multi-gap coaxial coils (MTMG-CCs) introduced in this work are flexible, form-fitting RF coils extending the concept of the single-turn single-gap CC by introducing multiple cable turns and/or gaps. It is demonstrated that this enables free choice of the coil diameter, and thus, optimizing it for the application to a certain anatomical site, while operating at the self-resonance frequency. An equivalent circuit for MTMG-CCs is modeled to predict their resonance frequency. Possible configurations regarding size, number of turns and gaps, and cable types for different B_0 field strengths are calculated. Standard copper wire loop coils (SCs) and flexible CCs made from commercial coaxial cable were fabricated as receive-only coils for 3 T and transmit/receive coils at 7 T with diameters between 4 and 15 cm. Electromagnetic simulations are used to investigate the currents on MTMG-CCs, and demonstrate comparable specific absorption rate of 7 T CCs and SCs. Signal-to-noise ratio (SNR), transmit efficiency, and active detuning performance of CCs were compared in bench tests and MR experiments. For the form-fitted receive-only CCs at 3 T no significant SNR degradation was found as compared to flat SCs on a balloon phantom. Form-fitted transmit/receive CCs at 7 T showed higher transmit efficiency and SNR. MTMG-CCs can be sized to optimize sensitivity, are flexible and lightweight, and could therefore enable the fabrication of wearable coils with improved patient comfort.**

***Index Terms*— Coaxial cable, flexibility, magnetic resonance imaging (MRI), MR physics, radio frequency (RF) coils, transmission line resonator (TLR).**

Manuscript received October 14, 2020; revised November 21, 2020; accepted January 9, 2021. Date of publication January 13, 2021; date of current version April 1, 2021. This work was supported in part by the Agence Nationale de Recherche (ANR) and Austrian Science Fund (FWF): I-3618 and in part by the Austrian/French OeAD/MAEE Project WTZ/PHC Amadée under Grant FR03/2018. *(Corresponding author: Elmar Laistler.)*

Lena Nohava is with the High Field MR Center, Center for Medical Physics and Biomedical Engineering, Medical University of Vienna, 1090 Vienna, Austria, and also with the Laboratoire d'Imagerie Biomédicale Multimodale Paris Saclay (BioMaps), CEA, CNRS, Inserm, Université Paris-Saclay, 91401 Orsay, France (e-mail: lena.nohava@meduniwien.ac.at).

Raphaela Czerny, Sigrun Roat, Michael Obermann, Roberta Frass-Kriegl, and Elmar Laistler are with the High Field MR Center, Center for Medical Physics and Biomedical Engineering, Medical University of Vienna, 1090 Vienna, Austria (e-mail: raphaela.czerny@gmail.com; sigrun.roat@meduniwien.ac.at; michael.obermann@meduniwien.ac.at; roberta.frass@meduniwien.ac.at; elmar.laistler@meduniwien.ac.at).

Andre Kuehne is with MRI.TOOLS GmbH, 13125 Berlin, Germany (e-mail: kuehne@mritools.de).

Jacques Felblinger is with the Inserm, IADI, Université de Lorraine, 54000 Nancy, France (e-mail: j.felblinger@chru-nancy.fr).

Jean-Christophe Ginefri is with the Laboratoire d'Imagerie Biomédicale Multimodale Paris Saclay (BioMaps), CEA, CNRS, Inserm, Université Paris-Saclay, 91401 Orsay, France (e-mail: jean-christophe.ginefri@universite-paris-saclay.fr).

This article has supplementary downloadable material available at https://doi.org/10.1109/TMI.2021.3051390, provided by the authors.

Digital Object Identifier 10.1109/TMI.2021.3051390

I. Introduction

In MAGNETIC resonance imaging (MRI), radio frequency (RF) coils are used to excite the nuclear magnetic moments, and to receive the MR signal at the Larmor frequency (f_{Larmor}) which is proportional to the static magnetic field (B_0). RF coils can be operated in receive-only mode if a separate transmit coil is available. For clinical MRI systems up to 3 T, this is a high-power body coil incorporated in the scanner bore. At ultra-high field (UHF, $\geq$ 7 T) [1]–[3], no such whole-body transmit coils are available. Therefore, transmit/receive (Tx/Rx) coils are often employed at UHF. In general, the target field of view (FOV) and penetration depth p determine the optimal coil size to be chosen for a certain biomedical application. Assuming a lossless circular coil, the coil diameter d_0 should equal $\frac{2p}{\sqrt{5}} \approx p$ to achieve optimal SNR in depth p inside a uniformly conductive sample [4]. Proximity to the target tissue is key for high magnetic coupling, resulting in high receive sensitivity and transmit efficiency. A high filling factor with the RF coil placed close to the sample results in less variation in coil performance due to varying loading conditions between different subjects and/or applications. Coils form-fitted to the average anatomy, e.g. for the human head, breast, calf or finger [5]–[8], have already been implemented with rigid

housings. However, weight, size and flexibility restrictions as well as suboptimal form-fitting in some cases are the drawbacks of these coils.

Flexible and stretchable RF coils are of great interest, as they can be closely fitted to the anatomy. The degree of flexibility depends on the respective design approach. Some investigations focused on coils with mechanically adjustable rigid or semi-flexible housing parts that can be wrapped around a 2D curved body contour [9]–[16]. Further improvement in flexibility was reached with printed and stitched coils on flexible substrate or even elastic textile. Screen-printed MRI coils [17] developed by Corea *et al.* have shown to be a reliable alternative to bulky conventional coils with comparable SNR, suitable especially for pediatric imaging [18]. Stretchable Rx coils produced with copper braids [19], [20], meandered conductors [21], liquid metal printed into neoprene support material [22], liquid metal filled tubes [23], [24] or conductive elastomers [25] mostly target wrist or knee imaging and offer a truly wearable solution.

In other studies targeting the fabrication of flexible RF coils, transmission line resonator (TLR) technology has been extensively employed [26]–[38]. All these approaches have in common that they are formed by at least two transmission line segments separated by gaps in one of the conductors. The TLR self-resonance is determined by the coil geometry and material properties (loop diameter, wire and substrate width, number of conductor turns and gaps, dielectric permittivity, etc.). In contrast to printed or braided copper structures, the advantage of self-resonant TLRs is that, ideally, e.g. when inductively matched and used in Tx/Rx mode, no lumped components with solder joints adding rigidity and losses are required. With capacitive matching and cabled connection to the MR system and depending on the coil function (Tx/Rx or Rx-only), still, some lumped components, e.g. for active detuning, are required either at the coil feed port or along the coil conductor. Initial MRI experiments with single parallel-plate TLR elements by Gonord *et al.* were conducted using a rigid dielectric substrate with a single-turn single-gap (1T1G) conductor deposited on both sides of the dielectric [39]. This was continued by the introduction of single-turn multi-gap (1TMG) TLR design to allow for larger coil diameters at UHF and multi-turn single-gap (MT1G) TLR design for small coils at UHF [40], [41]. So far, different flexible implementations of parallel-plate TLRs have been proposed: Ginefri *et al.* used small implantable multi-turn single-gap TLRs printed on a polymeric layer for rat brain MRI at 7 T [31]. Frass-Kriegl *et al.* extended the design to multi-turn multi-gap (MTMG) TLRs (MTMG-TLRs) which considerably increased the degree of freedom in parallel-plate TLR design [32]. Flexible coil arrays for 7 T were fabricated with single-turn multi-gap TLRs [13], [16]. Recently, a TLR structure of two parallel wire conductors encapsulated in a thin loop of dielectric material was proposed by Stormont *et al.,* which can be employed in blanket-like arrays [37].

Coaxial cable TLRs – with inner and outer conductor (cable shield) separated by a dielectric and gaps intersecting both conductors on opposite sides as for parallel-plate TLRs – have already been proposed as self-resonant RF coils by Zabel *et al.* for 1.5 T and Haziza *et al.* for low field [26], [27] and have recently been patented [33]. Equally as the embedded parallel-line TLRs in [37], coaxial coils (CCs) provide higher flexibility than parallel-plate TLRs; since they can be bent along a 3D curved body contour and therefore ideally form-fitted to the anatomy of interest, even with large inter-subject variability. Further, lightweight wearable array design and imaging of moving body parts becomes possible. CCs are especially interesting as some of the challenges arising in flexible coil development seem to be alleviated: they demonstrate robustness against coil deformation, load variation and inter-element coupling (overlap change) in an array configuration [29], [34], [38]. The re-occurring research interest in coaxial coil design has clearly been inspired by previous work on "shielded loop" (surface) [42], [43] and "coaxial cavity" (volume) resonators [44].

In 2018, Zhang *et al.* proposed 1T1G – "high impedance" – surface CCs to fabricate a wearable glove receive-array for 3 T MRI [34]. As the self-resonance frequency of a 1T1G-CC is given by the coil diameter and the properties of the chosen coaxial structure, the coil design is limited to one specific coil diameter in order to tune the self-resonance of the CC to the desired Larmor frequency. In the supplementary material of [34], the possibility to slightly vary the coil diameter with different cable properties, i.e. the dielectric constant of the substrate, cable thickness and characteristic cable impedance (depending on the ratio between outer and inner conductor thickness) is shortly discussed. No strict criteria to maintain flexibility were applied, i.e. also rigid dielectrics and cable thicknesses > 1 cm were considered, but still, the range of accessible diameters was very limited and not necessarily the optimum for a given anatomical application. With 1T1G-CCs, e.g. ^{1}H MRI of the breast can be realized at 3 T with a required coil diameter of approximately 8-10 cm to achieve the desired penetration depth. However, at 7 T, the 1T1G-CC diameter is restricted to a maximum of around 4-6 cm which can be suitable for human wrist/hand MRI or ex-vivo small animal imaging [30], [36] whereas at 1.5 T, the 1T1G-CC diameter is constrained to a minimum of 14-23 cm, only suitable e.g. for abdomen or pelvis imaging [35].

The purpose of this work is to explore the size limits of 1T1G-CCs and introduce and examine the extended design concept of coaxial coils with more than one gap and/or cable turns – multi-turn multi-gap CCs (MTMG-CCs) – as proposed by Laistler and Moser [45]. Some publications have suggested [46] or proven [29] the feasibility of introducing multiple gaps (at arbitrary positions) in the coaxial coil conductor to tune the surface coil to a desired resonance frequency. However, to the knowledge of the authors, this approach has never been investigated more systematically. Based on parallel-plate MTMG-TLRs [32], the goal is to increase the degrees of freedom in coaxial coil design, i.e. to allow for free choice of the CC diameter at any B_0 field to optimize the coil elements for the target application, which is not possible with 1T1G-CCs.

II. Materials and Methods

A. MTMG-CC Design Theory

In Fig. 1a, examples of CC layouts showing equidistant inner and outer gap positioning with one or multiple turns and/or gaps are given. The coil and cable parameters are specified in Fig. 1b and the equivalent circuit of a CC with an arbitrary number of turns and gaps is sketched in Fig. 1c.

In order to design and fabricate a CC, self-resonant at the target Larmor frequency, it is useful to formulate the resonance condition based on an equivalent circuit model. In measurements, the self-resonance can be determined inductively with a pick-up probe; in that case the CC can be seen as a series resonant circuit consisting of the impedances of the transmission line segments, and the inductance and resistance of the outer surface of the coax shield.

It is noteworthy that in a CC three distinct conductor parts can be identified, as illustrated in Fig. 1b: *iC*, the surface of the inner conductor; *oCi*, the inner surface of the outer conductor, and *oCo*, the outer surface of the outer conductor. The latter two are separated due to the skin effect at high frequencies and are only connected at the outer gaps. This way, the CC can be seen as transmission line segments formed by *iC* and *oCi*, interconnected via the inductance represented by *oCo*.

The total impedance Z_{tot} can, therefore, be estimated by the following equations:

$$X_{\mathrm{shield}}(\omega) = n_{\mathrm{t}}^2 \omega \mu_0 \frac{d_0}{2}\left[\ln\left(\frac{8d_0}{d_1}\right) - 2\right] \tag{1}$$

$$X_{\mathrm{TL}}(\omega) = -Z_0 \cot\left(\frac{\omega l \sqrt{\varepsilon_{\mathrm{r}}}}{c_0}\right) \tag{2}$$

$$Z_{\mathrm{tot}}(\omega) = R + i\left(X_{\mathrm{shield}}(\omega) + 2n_{\mathrm{g}} X_{\mathrm{TL}}(\omega)\right) \tag{3}$$

The inductive reactance X_{shield} is the classical approximation of the inductance of a conductive loop of the same diameter and thickness as *oCo* and is proportional to the squared number of turns (n_{t}) of the coaxial cable. The reactance X_{TL} of each transmission line segment is calculated with the classical formula for a lossless open-ended coaxial stub. The imaginary part of the total impedance Z_{tot} is the sum of the reactances of the outer shield and $2n_{\mathrm{g}}$ (twice the number of gaps) transmission line segments in series. The resonance condition is met, when the imaginary part of Z_{tot} disappears. Multiple resonances occur as the coaxial stub reactance alternates periodically with $\lambda/4$ between capacitive and inductive. In this work, only coils operated close to their first self-resonant mode f_0 are considered. The motivation to do so will be explained based on electromagnetic simulations in results section C.

From equations (1)-(3), the resonance frequency of the CC can be calculated in dependence of the coil diameter d_0, the number of turns n_{t} and gaps n_{g}, and the cable properties ε_{r}, d_1, and Z_0. The characteristic impedance Z_0 of a coaxial structure can be approximated and depends on the diameters of inner (d_2) and outer (d_1) conductor and the dielectric properties:

$$Z_0 = \frac{1}{2\pi}\sqrt{\frac{\mu_0}{\varepsilon_0 \varepsilon_{\mathrm{r}}}}\ln\left(\frac{d_1}{d_2}\right) \tag{4}$$

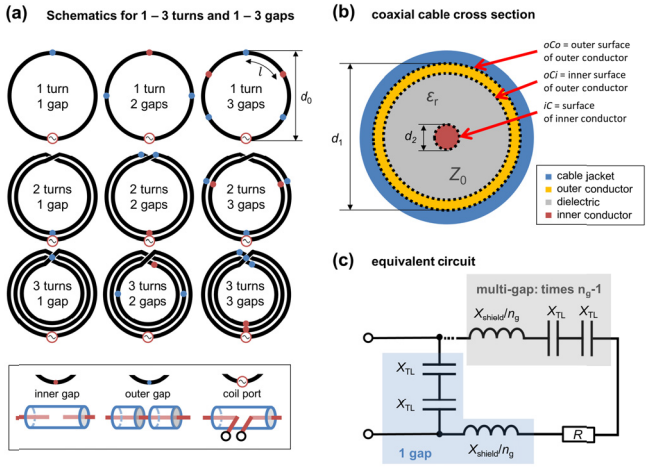

Fig. 1. Examples of gap positioning with 1-3 turns and 1-3 gaps (a), coaxial cable parameters (b), equivalent circuit model for an arbitrary number of turns (c), n_{g}, n_{t} …number of gaps and turns, d_0…coil diameter, l…length of one coaxial stub, d_1…outer diameter of outer conductor of coaxial cable, d_2…diameter of inner conductor, ε_{r}…relative permittivity, Z_0…characteristic cable impedance (Ω), X_{shield}…inductive reactance of the outer surface of the coax shield, X_{TL}…reactance of one coaxial stub (capacitive at resonance), R…resistance (ohmic coil losses). Although positioning of the port, depicted as a voltage source in (a), at the inner or outer gap would be equivalent in theory, it was always placed at inner gaps due to engineering considerations.

where μ_0 is the permeability of free space and ε_0 is the vacuum permittivity. For calculations in this work, Z_0 values given in the coaxial cable's data sheets were used and gap widths of 5 mm were taken into account for coaxial stub lengths. The high impedance of the CC (c.f. "high impedance coil (HIC)", Zhang *et al.* [34]) appears if the inner conductors at an inner gap are viewed as the coil port, since the first two coaxial stubs are then connected in parallel to the port and a parallel resonant circuit is formed (see also the schematic in Fig. 1c).

Since the electric and magnetic fields of a coaxial transmission line are confined to its inside, the part of the CC interacting with the environment is the outer surface of the shield, *oCo*. In the receive case, voltage is induced on the shield and, therefore, across the outer gap. In the transmit case, the excitation voltage at the CC port produces a current flow on the shield, which in turn creates the B_1^+ field.

B. Extension of Achievable Coil Diameter Range

To illustrate the extension of the achievable coil diameter range with MTMG-CCs as compared to 1T1G-CCs, the achievable coil diameters d_0 with self-resonant CCs were calculated using realistic value ranges for all coil and cable parameters (ε_{r}, d_1, Z_0, n_{t}, n_{g}, B_0). The reasoning for the limits for each parameter is detailed in Table I.

Using equations (1)-(3), numerical forward calculation of the resonance frequency f_0 was done in Matlab 2017b (The Mathworks, Inc., Natick, MA, USA). The parameter ranges from Table I were discretized for the calculations: the coil diameter range was sampled in 0.5 mm steps from 28.5 to 300 mm, resulting in 544 diameters. Five different cable

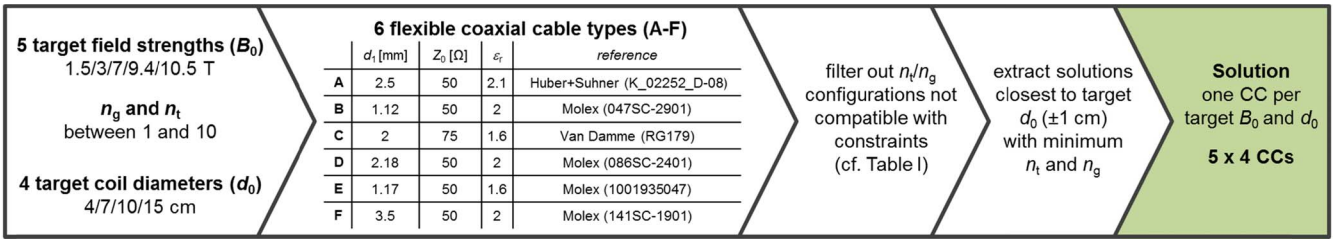

Fig. 2. MTMG-CC selection with commercial coaxial cables, specifying cable parameters (Z_0, d_1, ε_r) and references.

TABLE I
PARAMETER SPACE AND INEQUALITY CONSTRAINTS CONSIDERED IN THE CALCULATION OF THE ACHIEVABLE COIL DIAMETER RANGE FOR MTMG-CC VS. 1T1G-CCS

Parameter	Investigated range	Reasoning for limits
B_0 [T]	1.5, 3, 7, 9.4, 10.5	Common field strengths in MR
Characteristic impedance of coaxial cable Z_0 [Ω]	50, 75	Industry standards
Relative permittivity of cable dielectric ε_r	$1.2 \leq \varepsilon_r \leq 3.5$	Literature research on dielectric materials in commercially available flexible coaxial cables (min: foamed polyethylene, max: silicone rubber or polyvinyl chloride (PVC))
Dielectric diameter d_1 [mm]	$1\text{ mm} \leq d_1 \leq 3.5\text{ mm}$	The maximum dielectric diameter is approx. the diameter of the widely used RG58 cable, which was considered as the thickest cable that allows for sufficient flexibility. The minimum was determined by practical feasibility of gap construction and thin nonmagnetic cable availability.
Coil diameter d_0 [cm]	$d_{0,min} = \frac{9\text{ cm}}{\pi}$ $d_{0,min} \leq d_0 \leq 30\text{ cm}$	The minimum coil diameter is dictated by the minimum required length of cable segment to enable easy and reproducible fabrication of the gaps (experimentally determined: 9 cm) and $n_g = 1$, $n_t = 1$. The maximum was chosen to be 30 cm to possibly allow for the use as a transmit coil with a large FOV.
Number of turns n_t	$1 \leq n_t \leq 10$ (integer) $n_t \leq \frac{d_0}{8 \cdot d_1}$	Experimentally found constraint for flexibility, depending on coil diameter and cable thickness
Number of gaps n_g	$1 \leq n_g \leq 10$ (integer) $n_g \leq \frac{d_0}{d_{0,min}} \cdot n_t$	Limited by shortest possible cable segment (see "coil diameter").

parameter sets (each determined by ε_r, d_1, Z_0) were defined: two of these parameter sets were chosen to yield the minimum and maximum coil diameter, respectively, and three other cable parameter sets were added with intermediate parameter values. All 100 combinations of $n_t \leq 10$ and $n_g \leq 10$ were used. From the resulting $544 \times 5 \times 10 \times 10 = 272\,000$ coil variants, only the solutions obeying the inequality constraints regarding n_t and n_g from Table I, and those with resonance frequencies close to one of the five target Larmor frequencies (maximum $\pm$ 1 % deviation) were retained. The result of this theoretical approach is a range of possible coil diameters d_0 for each n_t/n_g CC configuration and B_0 field strength.

C. Realistic Coil Designs and Fabrication

In a second step, a more practical approach was pursued to select and fabricate CCs that are useful for different applications, and feasible in terms of non-magnetic flexible coaxial cable availability and geometry. The process to extract suitable CC solutions from the many calculations described in section B is summarized in Fig. 2.

For RF coils in the sample dominated noise regime, the SNR-optimum for a target penetration depth p is obtained with a d_0 approximately equal to p [4], the following four target coil diameters with respective possible biomedical applications were chosen: 4 cm (skin, hand, wrist), 7 cm (elbow, ankle, breast, head), 10 cm (breast, head, knee) and 15 cm (heart, abdomen). Further, 6 non-magnetic commercially available coaxial cable types were selected. For all cables, the outer conductor (shield) is thick enough to separate the currents on *oCi* and *oCo* over a frequency range from 50-500 MHz. The skin depth is always at least a factor of 10 smaller than the shield thickness. The steps to calculate d_0 for each target Larmor frequency, within a parameter space given by the cable types and n_g/n_t configurations, were the same as described in section B. Solutions with $\pm$ 1 cm maximum d_0 deviation from the target value and self-resonance frequency deviating $\pm$ 10 % from f_{Larmor} were kept. From these, the designs with the least number of gaps and turns were selected, since each gap is a potential breaking point even if covered with heat shrink tubing. Also, flexibility is reduced by soldering of the shield at inner gaps, heat shrink tubing, and by the number of turns. As a result, for each target field strength B_0 and target coil diameter d_0, one CC design was found that could be fabricated out of one of the 6 coaxial cable types, accepting the mentioned slight deviations between f_{Larmor} and the calculated f_0.

In this study, the 3 and 7 T ^{1}H coils from this design set were fabricated. The resulting eight (MTMG-)CCs had diameters of 4, 7, 10 and 15 cm, $n_{t,\max} = 2$ and $n_{g,\max} = 5$, and were fabricated from five different coaxial cables. Exact CC configurations and used cable types are detailed in results section B. For comparison, rigid standard coils (SCs) fabricated out of 1 mm copper wire and the same coil diameters as the CCs were constructed. All coils were tested on the bench and in MRI. For 3 T, Rx-only coils and for 7 T Tx/Rx coils were constructed.

Photographs and respective interface schematics of all fabricated coils are shown in Fig. 3. The interfacing circuitry at the coil port includes components for fine-tuning, matching and active detuning (AD) with PIN diodes (DH80106-10N, Cobham, Wimborne, UK) to decouple the 3 T Rx-only coils during transmission. A low-noise preamplifier (Hi-Q.A. Inc., Carleton Place, Ontario, Canada) was placed directly after the matching network of 3 T Rx-only coils. At 7 T, a transmit/receive (T/R) switch (Stark Contrast, Erlangen, Germany) with integrated low-noise preamplifier (Siemens Healthcare, Erlangen, Germany) was used to interface the coil to the scanner.

Rx-only CC interfaces were designed with a tuning inductor L_T which shifts the resonance to a higher frequency. In the loaded case, self-resonances f_0 of the CCs were generally lower than f_{Larmor} and a residual capacitive imaginary part of the impedance appeared at resonance that could be compensated with an inductor, as also explained in [34].

TABLE II
POSSIBLE CC CONFIGURATION (n_tTn_gG) AND CABLE TYPE (IN PARENTHESIS, SEE FIG. 2) PER B_0 AND COIL DIAMETER d_0

d_0 [cm]	B_0 [T]										
	1.5	3	7	9.4	10.5	3			7		
	CC configuration (cable type)					$f_{0,meas}$ [MHz]	$f_{0,calc}$ [MHz]	$f_{0,sim}$ [MHz]	$f_{0,meas}$ [MHz]	$f_{0,calc}$ [MHz]	$f_{0,sim}$ [MHz]
4	3T1G (E)	2T1G (D)	1T1G (B)	1T1G (C)	1T1G (C)	111.0	118.0 (+6.3 %)	111.0 (+0.0 %)	286.2	303.0 (+5.9 %)	287.3 (+0.4 %)
7	2T1G (A)	2T2G (E)	1T2G (B)	1T2G (F)	1T2G (C)	126.8	122.4 (−3.5 %)	125.6 (−1.0 %)	298.5	326.7 (+9.4 %)	309.2 (+3.6 %)
10	3T2G (C)	1T1G (A)	1T2G (C)	1T3G (F)	1T3G (C)	108.5	114.7 (+5.8 %)	109.0 (+0.5 %)	258.5	294.4 (+13.9 %)	276.2 (+6.9 %)
15	1T1G (B)	2T5G (B)	1T3G (C)	1T5G (A)	1T5G (C)	123.2	124.3 (+0.9 %)	115.6 (−6.2 %)	261.5	282.0 (+7.8 %)	263.4 (+0.7 %)

Fabricated and tested CCs are marked in light blue. On the right side of the table, f_0 measurements with the double-loop probe ($f_{0,meas}$) are compared to numerical calculations based on the equivalent circuit model ($f_{0,calc}$) and EM simulations ($f_{0,sim}$). Percentages in parenthesis indicate the respective relative deviation from $f_{0,meas}$.

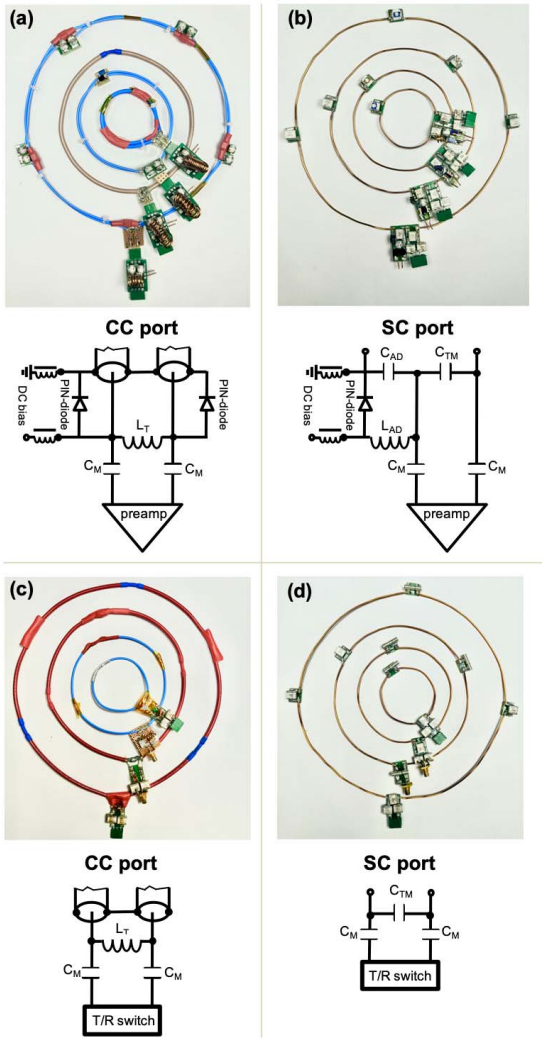

Fig. 3. Photographs of fabricated Rx-only CCs (a) and SCs (b) for 3 T and Tx/Rx CCs (c) and SCs (d) for 7 T and respective interface circuit schematics for tuning, matching and active detuning (only at 3 T). Note that the coils are only placed inside each other for the photograph, they are operated separately.

A tuning capacitor C_T instead of L_T would add to the coaxial stub capacitance (X_{TL}) and could therefore be used to lower the frequency if the self-resonance was higher than the target f_{Larmor}. Note that in work of Ruytenberg *et al.* [28], [38], purely capacitive tuning and matching is used for 10 cm Tx/Rx CCs with a first self-resonance of ≈ 110 MHz (see simulated and calculated values shown in Table II for a 10 cm 1T1G, cable A). For this coil example, with a tuning capacitor across the coil port (Fig. 1), the first parallel resonance mode measured across the port shifts to tens of MHz, whereas the second resonance mode shifts closer to the desired Larmor frequency, i.e. around 300 MHz. Therefore, due to the multiple resonances of a CC originating from the coaxial stub impedance behavior, the 1T1G-CC with a self-resonance $f_0 < f_{Larmor}$ used in [28], [38] can still be tuned and matched to 297.2 MHz with only capacitive components. To compare coil designs and motivate the use of a coil with an f_0 as close as possible to f_{Larmor}, the current distribution and amplitude along the *oCo*, depending on the coil geometry and operation frequency, was analyzed using electromagnetic simulation of the above-mentioned example of a 10 cm 1T1G-CC ($f_0 < f_{Larmor}$) compared to a 1T2G-CC used in this study ($f_0 \approx f_{Larmor}$), for $f_{Larmor} = 297.2$ MHz.

The determination of values for L_T and matching capacitors (C_M) for all CCs relied on S_{11} measurements of the unmatched and untuned loaded CC at the coil port using a vector network analyzer (VNA, E5071C, Agilent, Santa Clara, CA, USA). S_{11} measurements were exported for circuit simulation in ADS (Keysight Technologies Inc., Santa Rosa, CA, USA) where tuning (to f_{Larmor}) and matching (< -40 dB) components were determined. Inner gaps were constructed by cutting out ≈5 mm length of the inner conductor and to keep stability and a round coil shape, either heat shrink tubing was placed over the inner conductors close to the gap position or the inner conductors were bent away from the coil (with their isolating layer, especially with thin cables) and the outer conductors were soldered back together. Then again, heat shrink tubing was placed over the soldered outer conductor. Heat shrink tubing was also placed over the outer gaps for electrical insulation and mechanical stability. In CCs with multiple turns, insulating tape was wrapped around all cable turns to prevent f_0 shifts due to changes in the relative position of the individual cable turns.

The copper wire SCs were capacitively tuned (C_{TM}) and matched (C_M) and segmented by tuning capacitors along the loop at a length of maximum ≈ $\lambda/10$ to limit losses due to high electric fields [47].

D. Electromagnetic Simulations

Simulations of all implemented CCs were performed using the finite element solver of CST Studio Suite 2020 (Dassault Systèmes, Paris, France). Curved surfaces were approximated using second order finite elements. For accurate results, adaptive mesh refinement was used, with the S-parameter convergence criterion set to 0.001. Broadband results were generated using the general-purpose broadband sweep method of CST with a maximum S-parameter interpolation error of 0.001, which allowed to extract a broadband response between 50 and 500 MHz using approximately 10 frequency samples. In a first simulation run, the self-resonances f_0 of the unloaded coax loops were determined by finding the first local maximum of $|Z|$. In a second run, 3D current monitors were placed at these frequencies in addition to monitors covering the respective target Larmor frequency. Subsequently, surface current density ($K = \mathrm{d}I/\mathrm{d}l$) as well as S-matrices were exported for further analysis. Forward power was set to 0.5 W. Multi-turn coils were modeled as helical structures, where outbound wires at the start and end were used in order to close the coil without crossing the coaxial line in between (Fig. 6b). Further, CCs and SCs designed for Tx/Rx use at 7 T were simulated in loaded configuration. The box-shaped phantom dimensions were adapted depending on the coil diameter ($4d_0$ cm $\times$ $4d_0$ cm $\times$ 25 cm), electrical properties set to a conductivity of $\sigma = 0.6$ S/m and permittivity of $\varepsilon_r = 80$ and the phantom placed at 0.5 cm from the coil.

Post-processing of the simulated data was performed with Matlab 2017b. Simulations were scaled to 1 W accepted input power (P_{acc}), taking into account the respective reflection coefficients (S_{11}) from simulation. The surface current density K was analyzed on the three mentioned conductor parts iC, oCi, and oCo. The surface current I was derived by integrating K over volumes along the structures of a length of 1 mm. Multiplication with the respective conductor diameter yields the surface current I. The outbound wires for the multi-turn CCs were excluded from the surface current evaluation. Specific absorption rate (SAR) was calculated pointwise and 10 g averaged from simulated E-field data over the whole phantom. Maximum intensity projections (MIPs) of the point SAR in the coronal plane, i.e. parallel to the coil plane, and SAR efficiency ($B_1^+/\sqrt{\text{max. 10g SAR}}$) maps in all planes (sagittal and transversal through the coil's center, coronal at a distance $d_0/4$ from the coil) were calculated for 7 T CCs and SCs. Maximum 10 g and point SAR values per 1 W P_{acc} were extracted and mean transmit efficiency (mean $B_1^+/\sqrt{P}$) as well as mean SAR efficiency (mean $B_1^+/\sqrt{\text{max. 10g SAR}}$) were calculated in a half-spherical volume of interest with its center at the coil center, and a diameter equal to d_0 to yield quantitative measures for comparison between CCs and SCs.

E. Bench Measurements

Phantoms used in bench tests and MRI experiments are shown in Fig. 4. A 5- or 25-liter container phantom (Fig. 4a) was used for measurements where the coils were placed in a flat configuration on the phantom surface. Measurements with bent coils were performed using a 3D-printed holder-set

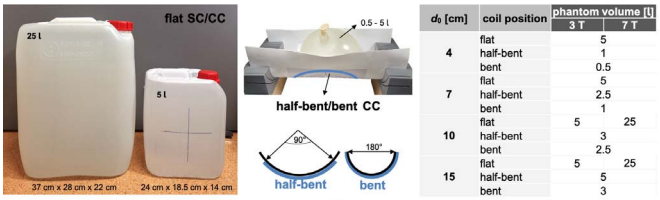

d_0 [cm]	coil position	phantom volume [l] 3 T	7 T
4	flat	5	
	half-bent	1	
	bent	0.5	
7	flat	5	
	half-bent	2.5	
	bent	1	
10	flat	5	25
	half-bent	3	
	bent	2.5	
15	flat	5	25
	half-bent	5	
	bent	3	

(c)

Fig. 4. Bench and MR measurement set-up: container phantoms used for flat measurements (a), holders with PTFE plate and balloon phantom to simulate two bending scenarios (b), phantom volumes used per coil size and coil position (c).

up with slits to place a bent polytetrafluoroethylene (PTFE) sheet and balloon phantoms of different sizes depending on the target application and bending radius (Fig. 4b). The average bending case ("half-bent") was defined as opposite coil conductor ends spanning a 90° angle and in the maximum assumed bending case ("bent"), coil ends span a 180° angle in the cross-section, as shown in Fig. 4b.

All phantoms were filled with saline solution (1.6 g NaCl/l deionized water) with a DC conductivity of 0.2 S/m, and doped with 1 ml/l Gd-based contrast agent to shorten acquisition time. For 3 T measurements, all coils were directly placed on or under the phantom. The same applies for 7 T measurements, except for the 15 cm coils, which were placed at 1 cm distance from the sample using a foam spacer, in order to reduce loading.

Bench tests were performed using the VNA. First, the self-resonance frequency of CCs was measured inductively with a decoupled double-loop probe (baseline value < -80 dB) [48] without interface. SCs were tuned by distributed capacitors. Inductive measurements were performed with SCs and CCs in flat position and CCs in half-bent and bent position. For these coil setups, the unloaded and loaded resonance frequency ($f_{0,\mathrm{u}}$ and $f_{0,\mathrm{l}}$) and quality factor ($Q_{0,\mathrm{u}}$ and $Q_{0,\mathrm{l}}$), respectively, were determined. Copper wire SCs cannot be reversibly bent, therefore, only CCs were investigated in bent configuration.

Coils with interfaces were connected to the VNA via their 50 Ω matching circuit and using a custom-built test rig to mimic the MR scanner's coil connectors including DC supply to switch either the AD circuit or the transmit/receive switch. All coils were initially tuned and matched in flat position on the container phantom with a volume listed in Fig. 4c. S-parameter measurements (S_{11} in dB) of the matching level at f_{Larmor} were carried out to track changes during CC bending and characterize the behavior in two different bending scenarios with different balloon phantom sizes, also measuring $f_{0,\mathrm{l}}$ and Q_{l}. In a next step, the coils were re-tuned and re-matched to be used in either flat position (SC) or bent position (CC) on a balloon phantom (see Fig. 4b). Again, the matching level at f_{Larmor} and Q_{loaded} was measured. With the test rig, the functioning of AD components in the Rx-only coils was verified: for SCs the AD circuit was tuned to f_{Larmor} to efficiently block currents at this frequency and for CCs, the switching of all PIN diodes between tuned and detuned state was checked.

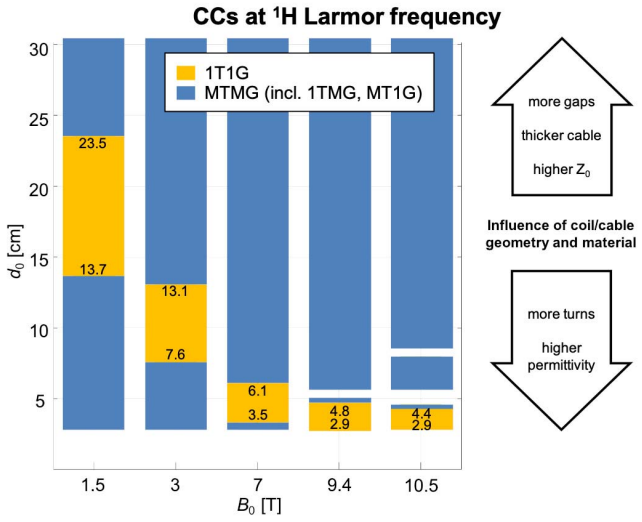

Fig. 5. Possible CC diameters (d_0) at the ^{1}H Larmor frequency for 5 different common field strengths using realistic coil and cable parameters (see Table I). The diameters that can be achieved with 1T1G coils are marked in yellow, the diameters only accessible with multiple turns and/or gaps are marked in blue. Due to the discrete nature of some of the parameters, small voids in the diameter ranges at 9.4 and 10.5 T can be observed.

F. MRI Experiments

MRI experiments were carried out on a 3 T and a 7 T MR scanner (Prisma Fit and 7 T Magnetom, Siemens Healthineers, Erlangen, Germany) in the following setups: SCs and CCs in flat position on a container phantom, and SCs in flat and CCs in bent position on a balloon phantom. The aim was to compare CCs and SCs in terms of SNR performance (3 T and 7 T), and evaluate transmit efficiency (7 T only).

At 3 T, gradient-echo (GRE) images were acquired in a transversal slice through the coil center (scan parameters: T_R/T_E = 50/10 ms, FOV = 290 × 290 mm^2, 0.6 × 0.6 mm^2 in-plane resolution, 6.5 mm slice thickness). Data from GRE scans were used to calculate SNR maps and to evaluate SNR in a circular ROI with diameter $d_0/4$ centered underneath the coil. The distance D between coil and ROI center was 1, 2.5, 4 and 5.5 cm for the 4, 7, 10 and 15 cm coil, respectively. Relative SNR difference maps for the CC vs. the SC on a balloon phantom were calculated as $SNR_{CC}/SNR_{SC} - 1$.

To determine the reliability of AD circuits in CCs and SCs, we performed flip angle mapping with and without the Rx coil present in flat position, using the body coil for Tx/Rx. From these data, the relative flip angle difference maps with vs. without Rx coil were calculated. Efficient decoupling from the body coil in Rx-only CCs has already been demonstrated in single-gap CCs [34]. To test this for coils with multiple gaps, measurements of the flip angle distribution (saturated Turbo FLASH [49]) with and without the detuned MTMG coil present were performed. The transmission decoupling performance of the coil with the highest number of gaps in the study (2T5G-CC) with only one pair of detuning PIN diodes at the coil port, was compared to another one with a pair of PIN diodes at each of the inner gaps. In the latter case, at every outer gap an RF choke (1812CS, Coilcraft, Cumbernauld, UK) was placed to provide the DC connection for biasing the PIN diodes (see photograph in Fig. 3a).

At 7 T, flip angle maps in the central sagittal slice were acquired, using the saturated Turbo FLASH method [49]. The excitation pulse amplitude V_{ref} was adjusted to achieve an average flip angle of 90° in a ROI with diameter $d_0/4$ and the ROI center at a distance D from the coil center in flat position (D = 1, 2, 2.2, 2.7 cm for the 4, 7, 10 and 15 cm coil, respectively). For the balloon phantom and the SC in flat or the CC in bent position, the pulse amplitude V_{ref} was again adjusted to obtain a 90° flip angle in the same ROI. $B_1^+/\sqrt{P}$ maps, i.e. the RF transmit field normalized to the input power, indicating the transmit efficiency, were calculated from flip angle maps and the respective pulse parameters. GRE images were also acquired in the central sagittal slice (scan parameters: T_R/T_E = 50/4.8 ms, in-plane resolution 0.5 × 0.5 mm^2, FOV = 256 × 256 mm^2, 3 mm slice thickness). As the flip angle in the ROI was kept constant for each coil setup, SNR evaluation in the same ROI allows comparison of the coil's receive sensitivity contribution only. Relative SNR and $B_1^+/\sqrt{P}$ difference maps for the CC versus the SC on a balloon phantom were calculated.

III. Results

A. Extension of Achievable Coil Diameter Range

Fig. 5 illustrates the possible coil size ranges for 1T1G (yellow) versus MTMG-CCs (blue) within the chosen parameter space detailed in Table I. As can be seen, 1T1G-CCs are limited to large coils at low field and small coils at high field. Allowing for multiple turns and/or gaps, the possible diameter range starts at approximately 3 cm for all B_0 field strengths. The range is almost continuous up to 30 cm in diameter and discontinuities only appear at ultra-high field. In practice, commercially available coaxial cables only cover the assumed continuous range for permittivity and cable diameter discretely, and therefore obviously leading to discrete achievable CC diameters. These, however, still offer sufficient freedom in choice of the coil size to obtain results close to the target coil size. On the right side of Fig. 5, the arrows indicate how coil and cable parameters influence the coil size.

B. Realistic Coil Designs

In Table II, realistic design parameters for the fabrication of CCs made from non-magnetic commercially available flexible coaxial cable types are listed for different B_0 fields and target d_0 with their self-resonance as close as possible to the target f_{Larmor}. The deviations from the measured resonance frequency are < 13.9 % for calculated and < 6.9 % for the simulated values. Note that the values for $f_{0,meas}$ here differ from the unloaded values in supplementary Table I,[1] since they were obtained without AD components or interface connector on the coil.

[1]Supplementary materials are available in the supporting documents /multimedia tab.

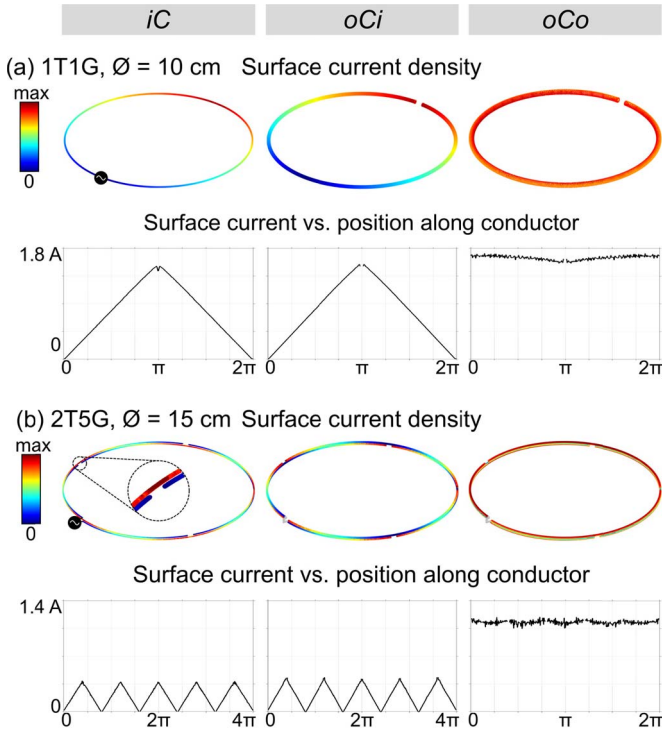

Fig. 6. Surface current density and surface current simulation results. Two representative simulation results are shown to depict the coaxial coils' behavior for a (a) single turn single gap, (1T1G, $d_0 = 10$ cm, $f_0 = 109$ MHz) and (b) a multi turn multi gap (2T5G, $d_0 = 15$ cm, $f_0 = 115.6$ MHz) at their respective self-resonances f_0. The surface current densities K at f_0 are depicted as 3D plots for *iC*, *oCi*, and *oCo*, scaled to their individual maximum. The corresponding magnitudes of the surface currents $|I|$ along the coil windings are shown as line plots, starting from 0 at the feed point to $n_t \times 2\pi$ in the case of *iC* and *oCi*. The current on *oCi* has opposite direction to its mirror-current on *iC*. For *oCo*, the surface current was integrated over all turns, since this represents the effective current seen at distance from the coil, and the plot only goes to 2π. The feeding and necessary connecting structures to avoid self-intersection of the geometry are depicted in grey/black.

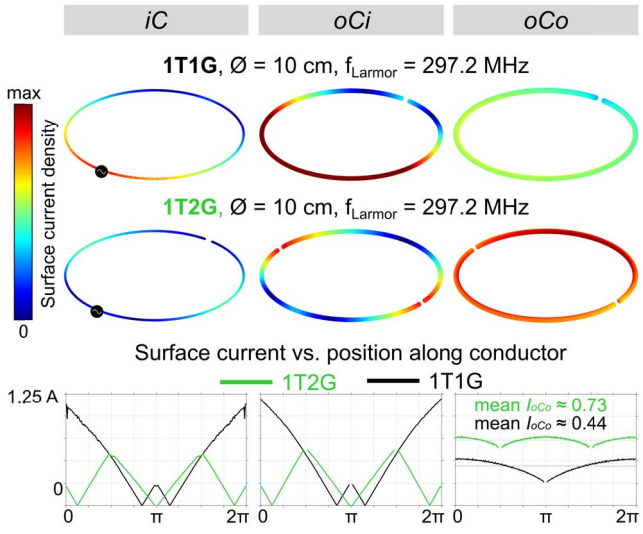

Fig. 7. Surface current density and surface current simulation results for a 10 cm 1T1G-CC compared to a 1T2G-CC of same size.

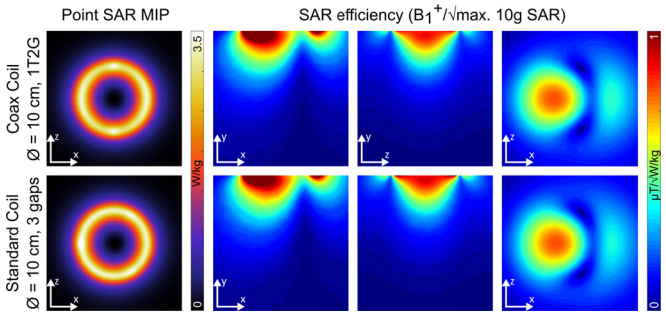

Fig. 8. Point SAR MIPs (W/kg) and SAR efficiency ($B_1^+/\sqrt{}$W/kg) maps calculated from EM simulation results for a 10 cm CC and SC used at 7 T.

C. Electromagnetic Simulations

Fig. 6 shows simulation results of a 1T1G (a) and a MTMG (b) CC at their respective self-resonances f_0. Results for all investigated coils (blue area in Table II) at their target Larmor frequency f_{Larmor} are shown in supplementary Fig. 1[1]. The typical transmission line behavior can be observed for *iC* and *oCi*, where the current on *iC* is the mirror-current of the current on *oCi*, with a maximum in current density magnitude at each outer gap and a zero at each inner gap. However, the current along *oCo,* which corresponds to the effective current seen at distance from the coil, is rather constant along the conductor.

The motivation to use a CC with a first self-resonance as close as possible to the Larmor frequency which is the case for all MTMG-CCs employed in this work, is illustrated with the example shown in Fig. 7. Both coils have a diameter of 10 cm and are simulated at a Larmor frequency of 297.2 MHz. The 1T1G-CC geometry was chosen according to details given in [38] (cable A) and has a simulated $f_{0,\text{sim}}$ of 109.0 MHz. The 1T2G-CC used in this work has an $f_{0,\text{sim}}$ of 276.2 MHz (see Table II). Simulation results of the surface current density and surface current I in Fig. 7 are in agreement with the ones shown for the 1T1G-CC in [38] and demonstrate that, scaled to 1 W accepted power, I along the *oCo* is higher in amplitude and more homogeneous for the 1T2G-CC.

SAR simulations targeted the comparison between SCs and CCs used in Tx/Rx mode at 7 T. Fig. 8 shows a representative simulation result for a 10 cm CC and SC, i.e. SAR MIPs in the coronal (xz) plane and SAR efficiency maps in a transversal and sagittal slice through the coil center as well as in a coronal slice (at a distance of 2.5 cm from the coil). The coaxial coil in this example has two gaps and the standard coil is segmented by three capacitor "gaps". In supplementary Fig. 2[1], SAR simulation results for all CCs and SCs (8 in total) are presented. Table III summarizes maximum local 10 g SAR, maximum point SAR, mean transmit (TE) and mean SAR (SE) efficiency values for all 7 T CC and SCs. All maps and parameters are very similar for the 7, 10 and 15 cm SCs and CCs. The 4 cm SC has slightly lower maximum local 10 g SAR and higher mean TE, i.e. also higher SE than the CC, although still comparable in performance (see supplementary Fig. 2[1]).

D. Bench Measurements

Bench measurement results for 3 T and 7 T SCs and CCs without and with interface, different coil positions, and tuning and matching configurations are summarized in supplementary

TABLE III
7 T SIMULATION RESULTS FOR ALL CCS AND SCS

d_0 [cm]		max. 10 g SAR	max. point SAR	mean TE	mean SE
	coil type	W/kg per 1 W P_{acc}	W/kg per 1 W P_{acc}	$\mu T/\sqrt{W}$	$\mu T/\sqrt{W/kg}$
4	CC	5.04	17.05	4.33	1.93
	SC	4.69	15.61	4.53	2.09
7	CC	2.85	6.56	1.56	0.92
	SC	2.87	6.84	1.58	0.93
10	CC	1.81	3.43	0.84	0.62
	SC	1.81	3.78	0.86	0.64
15	CC	1.03	1.89	0.45	0.44
	SC	1.01	2.14	0.46	0.46

Table I[1]. For Rx-only CCs at 3 T with multiple gaps (7 and 15 cm CCs), AD PIN diodes lead to a relatively low Q_u due to added ohmic losses but CCs still operate in the sample noise dominated domain. From Q_u and Q_l values measured for CCs in flat position without interface, we can conclude that the frequency-normalized coil losses R_C scale with $d_0 n_t^2$ and the frequency-normalized sample losses R_S scale with $d_0^3 n_t^2$ in accordance with equations 8 and 9 given in [50]. Generally, Q_u of CCs is comparable or lower as for SCs and Q_l of CCs is comparable or higher as for SCs. Therefore, the Q-ratio (Q_u/Q_l) is mostly lower for CCs than for SCs. At both 3 and 7 T, for both coil types, different coil setups (flat, half-bent, bent) and phantom volumes (container, balloons) the Q-ratios were always superior to 2, demonstrating coil operation in a sample noise dominated regime.

In flat and loaded coil configuration, SCs and CCs with their interfaces were tuned to the respective f_{Larmor} and matched to a level better than −18.4 dB. During CC bending, either to half-bent or bent position, $f_{0,l}$ increases. Thus, matching at f_{Larmor} is degraded. The higher Q_l and the higher $\Delta f_{0,l}$, the stronger the observed degradation in matching. For some CCs, re-tuning and re-matching to the balloon phantom is indispensable. The CCs with 15 cm diameter at 3 T and the ones with 7, 10, and 15 cm at 7 T were acceptably matched even during strong bending (assuming a threshold of −8 dB/15 % reflected power). During re-tuning and re-matching of SCs in flat and CCs in bent position on the balloon phantom, matching levels better than −15 dB were reached.

E. MRI Experiments

At 3 T, flip angle mapping results with a 2T5G-CC using an AD circuitry consisting of PIN-diodes shorting inner and outer conductor only at the coil port (see circuit scheme in Fig. 3a) reveal non-sufficient decoupling of Rx and body coil with relative flip angle changes of over 60 % shown in Fig. 9b. With an AD network consisting of a set of PIN diodes at every inner gap and RF chokes connecting the outer gaps (Fig. 9a), reliable AD is ensured as any residual resonances are eliminated (Fig. 9c). For all SCs and CCs used in this study, the relative flip angle difference without vs. with Rx coil present is < 10 – 20 % over the whole phantom.

3 T SNR maps are presented in Fig. 10. All images shown in Fig. 10 and Fig. 11 were cropped to the respective coil size. In flat position, the average SNR in a circular ROI is lower for CCs as compared to SCs (−48.6 %, −33.9 %, −28.2 % and −17.1 % for the 4, 7, 10 and 15 cm CC, respectively). Using the CC bent to the balloon phantom compared to a flat SC results in a moderate SNR gain or slightly lower SNR in the ROI (−2.3 %, +10.8 %, +7.0 % and −5.7 % for the 4, 7, 10 and 15 cm CC, respectively), as also shown in relative SNR difference maps in Fig. 10.

At 7 T, transmit efficiency $B_1^+/\sqrt{P}$ maps presented in Fig. 11a show good comparability of SCs and CCs in flat measurements as the same pulse amplitude was needed for SCs and CCs to achieve a 90° average flip angle in the circular ROI (V_{ref} = 25, 63, 130 and 200 V for the 4, 7, 10 and 15 cm coils, respectively). $B_1^+/\sqrt{P}$ between CC and SC only slightly differs by +2.5 % (4 cm), +3.2 % (7 cm), −0.8 % (10 cm) and −2.4 % (15 cm). On the balloon phantom, with the SC in flat position and the CC bent to the balloon, lower V_{ref}

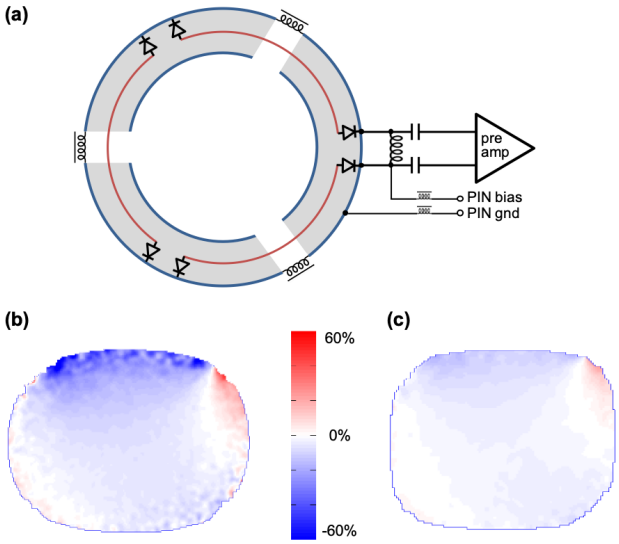

Fig. 9. Active detuning components with multiple gaps (arbitrary nt): (a) inner gaps need to be shorted by PIN diodes and outer gaps connected by RF chokes. Relative flip angle difference maps for a 2T5G 15 cm diameter CC at 3 T (b) detuned only at the port or (c) at every inner gap.

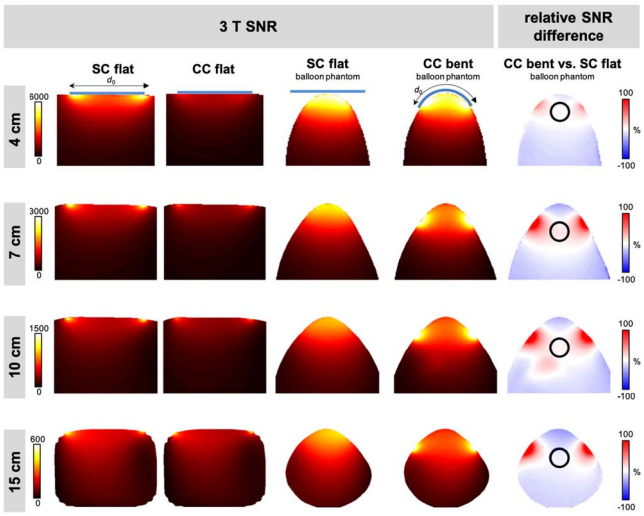

Fig. 10. 3 T MRI results, SNR maps in the central transversal slice for the 4, 7, 10 and 15 cm SC and CC in flat position on a container phantom and the SC in flat and the CC in bent position on a balloon phantom, relative SNR difference maps.

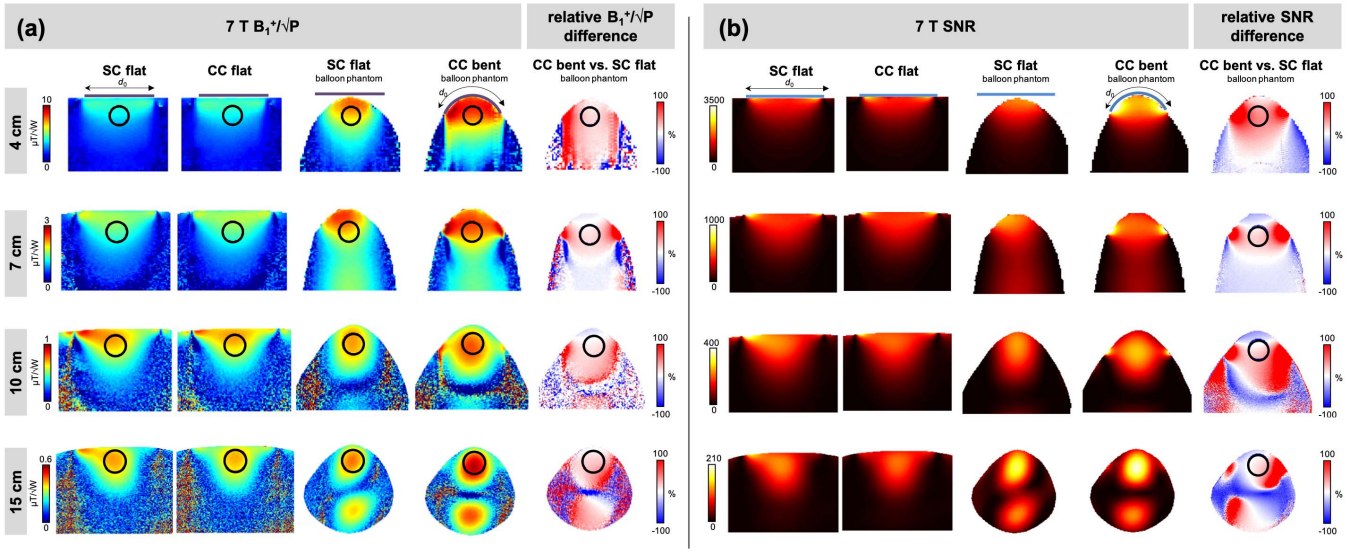

Fig. 11. 7 T MRI results, $B_1^+/\sqrt{\text{P}}$ maps (a) and SNR maps (b) in the central sagittal slice for the 4, 7, 10 and 15 cm SC and CC in flat position on a container phantom and the SC in flat and the CC in bent position on a balloon phantom, relative $B_1^+/\sqrt{\text{P}}$ and SNR difference maps (CC vs. SC on balloon phantom).

than for flat measurements on the container were required to achieve 90° average flip angle in the ROI ($V_{\text{ref,SC}} = 12.5$, 44, 123, 193 V and $V_{\text{ref,CC}} = 11$, 38, 112, 160 V). CCs in bent configuration showed higher transmit efficiency than the flat SC with a gain in $B_1^+/\sqrt{P}$ of +17.1 %, +14.8 %, +9.1 % and +21.9 % for the 4, 7, 10 and 15 cm CC, respectively (Fig. 11a). 7 T SNR maps demonstrate that, in flat position, the average SNR in a circular ROI is comparable or slightly lower for CCs as compared to SCs (+0.5 %, +1.1 %, −8.1 % and −6.9 % for the 4, 7, 10 and 15 cm CC, respectively), see Fig. 11b. However, when CCs are form-fitted to the balloon and compared to the flat SCs, a considerable SNR gain can be observed (+40.5 %, +18.0 %, +11.1 % and +10.6 % for the 4, 7, 10 and 15 cm CC, respectively), see Fig. 11b.

Standing wave patterns occurring in both $B_1^+/\sqrt{P}$ and SNR maps, which are more pronounced for larger coil sizes, can be explained by the electrical properties and dimensions of the phantom. For a wavelength (≈11 cm) smaller than the phantom size and low sample conductivity, resulting in a skin depth larger than the phantom size, the forward and reflected wave can create EM interference patterns. Alternatively, dielectric phantom resonances could be the cause for standing wave patterns [51].

IV. Discussion and Conclusion

In this work, the design concept for multi-turn multi-gap coaxial RF coils is presented. An equivalent circuit is modeled; theoretical solutions for CCs are calculated for five common B_0 field strengths and different coil sizes. Surface current density simulations are performed to analyze the three distinct conductor parts of a CC. SAR simulations conducted for 7 T Tx/Rx CCs and SCs demonstrate similar performance of both coil types. The study focused on a proof-of-concept of employing (MTMG-)CCs in Rx-only mode at 3 T and Tx/Rx mode at 7 T MRI. CCs with 4, 7, 10 and 15 cm coil diameters were fabricated from commercially available non-magnetic coaxial cables. During bench and MRI tests, they demonstrate robustness upon bending as well as $B_1^+/\sqrt{P}$ and SNR improvement (7 T) or no significant SNR loss (3 T) when form-fitted to a balloon sample as compared to flat standard copper loop coils.

One of the causes for deviations between measured, calculated and simulated f_0 is most likely the limited accuracy of handmade gap construction, where asymmetries and gap length variations might shift f_0. Also, the equivalent circuit model does not account for stray capacitance at the gaps. The fabricated CC geometries slightly deviate from simulated ones, e.g. the multi-turn CC geometry was modeled as a helical structure and the conductor material was assumed to be solid copper for all coils although some conductors may in reality be braided and/or coated by other materials. Nevertheless, calculated resonance frequencies sufficiently match the measured results, so that the equivalent circuit was deemed valid to be used for finding suitable MTMG-CC designs for a target resonance frequency and desired coil diameter. In the choice of coaxial structures used in this work, an emphasis was put on flexibility and commercial availability of the cable. This comes with advantages, e.g. easier reproducibility and fast prototyping but also with drawbacks, e.g. soldering joints along the loop to re-connect the outer conductors at inner gaps. However, in principle also semi-rigid or rigid coaxial structures (commercial or custom 3D printed) or other elaborate techniques for flexible coaxial structure manufacturing could be used for coil fabrication. In that case, e.g. the cable impedance could be varied in an even larger range and the CC resonance could be more precisely tuned for a given coil diameter. Furthermore, solder joints along the loop could be avoided with customized manual assembling of inner conductor and outer conductor with beforehand introduced gaps, and a separating dielectric.

Clearly, additional active detuning components required for multi-gap coils operating in Rx-only mode impair flexibility, lead to suboptimal coil robustness and increase coil noise. Nevertheless, we believe it is interesting to show the proof-of-concept of fabricating MTMG-CCs for Rx-only use at 3 T and the implications of introducing multiple gaps on the active detuning reliability, not least to ensure patient safety when experimenting with this novel coil design concept. The multi-gap design is certainly more advantageous for Tx/Rx coils where additional active detuning components are not needed. When employed at UHF $\geq$ 7 T, where standard coils would require many segmenting capacitors, stub segments between gaps in multi-gap CCs become shorter (in contrast to the single-gap coil of same size), yielding homogeneous current distribution on the outer surface of the outer coaxial conductor (see Fig. 7), similar Tx/Rx performance (see Fig. 11) and SAR efficiency (Fig. 8, supplementary Fig. 2[1]) compared to rigid segmented copper loops.

The characteristics of single-element (MTMG-)CCs could be more ideally exploited in array configuration: the size-optimized CC elements achieving optimal SNR in the target penetration depth, combined with large FOV coverage of an array would result in a flexible, light-weight coil improving patient comfort and image quality compared to rigid arrays with large variations in sample-coil distance. Also, in array configuration, depending on the application, the single element coil radius may be rather small and therefore single elements not necessarily as strongly bent as demonstrated in this work. Furthermore, in practice, the baseline bending and loading configuration for coil matching can be changed from flat to a certain average bending and a more specific load depending on the anatomical application.

For *in vivo* use of Tx/Rx MTMG-CCs EM simulations are required to estimate the specific absorption rate. These simulations should ideally be based on a finite element method (FEM) solver due to the fine sub-millimeter structures involved, as also employed for EM simulations presented in this work. For heavily populated coil arrays, the computational complexity could potentially become unfeasible to be computed with a FEM solver, due to the sophisticated meshing necessary to resolve the coil structures and a human sample. As demonstrated in this work, CCs could be approximated by standard loops for H- and E-field simulations, since it was shown here that the current interacting with the sample and neighboring coils (on the outer surface of the outer conductor) is rather uniform and EM simulation results on SAR and transmit efficiency were comparable between SCs and CCs at 7 T. Large CCs $>$ 20 cm not fabricated in this work could be interesting for use as Tx coils at 7 T although other coil types (e.g. dipoles alone or combined with loop coils) might be more advantageous for large penetration depths at UHF [52], [53]. Although a homogeneous current distribution along the *oCo* was targeted in this work (as with most segmented standard coils), it is conceivable that a non-uniform placement of the gaps leading to unbalanced current distribution on the *oCo* [29] could also be exploited at UHF, in analogy to "loopole" designs [54], [55] which combine loop and dipole antenna properties. The 1T1G coil shown in Fig. 7 (see also [38]), operating far from its self-resonance can cause a similar "loopole"-type current distribution and might yield improved performance compared to a simple loop coil, depending on the coil orientation relative to B_0 [54]. Furthermore, the asymmetric current pattern might be an explanation [55] for improved inter-element decoupling observed in references [29], [38].

As a future perspective, tracking of the flexible coils using MR-visible materials contained in the outer cable jacket [56] can be envisioned, possibly useful for localized on-coil B_0 shimming or motion correction.

In conclusion, the major asset of MTMG coaxial coils presented in this work is their low weight, flexibility, and the fact that the coil size can be chosen (almost) freely for various B_0 field strengths. Implementing the MTMG principle, the size-restriction of 1T1G-CCs can be overcome, and CC elements can be size-optimized for a wide range of anatomical applications. The high flexibility of CCs especially benefits applications where inter-subject variability is strong (breast, abdomen, joints, heart etc.) and where standard rigid coils would usually be placed far away from the anatomy of interest. Furthermore, the low weight and flexibility allows the fabrication of versatile, "wearable" coils, increasing patient comfort.

REFERENCES

[1] E. Moser, "Ultra-high-field magnetic resonance: Why and when," *World J. Radiol.*, vol. 2, no. 1, pp. 37–40, 2010.

[2] E. Moser, F. Stahlberg, M. E. Ladd, and S. Trattnig, "7-T MR-from research to clinical applications?" *NMR Biomed.*, vol. 25, no. 5, pp. 695–716, May 2012.

[3] E. Moser, E. Laistler, F. Schmitt, and G. Kontaxis, "Ultra-high field NMR and MRI-the role of magnet technology to increase sensitivity and specificity," *Frontiers Phys.*, vol. 5, p. 33, Aug. 2017.

[4] A. Kumar, W. A. Edelstein, and P. A. Bottomley, "Noise figure limits for circular loop MR coils," *Magn. Reson. Med.*, vol. 61, no. 5, pp. 1201–1209, May 2009.

[5] A. N. Nnewihe *et al.*, "Custom-fitted 16-channel bilateral breast coil for bidirectional parallel imaging," *Magn. Reson. Med.*, vol. 66, no. 1, pp. 281–289, Jul. 2011.

[6] K. M. Gilbert, J.-G. Belliveau, A. T. Curtis, J. S. Gati, L. M. Klassen, and R. S. Menon, "A conformal transceive array for 7 T neuroimaging," *Magn. Reson. Med.*, vol. 67, no. 5, pp. 1487–1496, May 2012.

[7] E. Laistler *et al.*, "*In vivo* MRI of the human finger at 7 T," *Magn. Reson. Med.*, vol. 79, no. 1, pp. 588–592, Jan. 2018.

[8] S. Goluch *et al.*, "Proton-decoupled carbon magnetic resonance spectroscopy in human calf muscles at 7 T using a multi-channel radiofrequency coil," *Sci. Rep.*, vol. 8, no. 1, p. 6211, Dec. 2018.

[9] W. Kwok, "A volume adjustable four-coil phased array for high resolution MR imaging of the hip," *Magn. Reson. Mater. Biol., Phys., Med.*, vol. 9, nos. 1–2, pp. 59–64, Oct. 1999.

[10] G. Adriany *et al.*, "A geometrically adjustable 16-channel transmit/receive transmission line array for improved RF efficiency and parallel imaging performance at 7 Tesla," *Magn. Reson. Med.*, vol. 59, no. 3, pp. 590–597, Mar. 2008.

[11] J. A. Nordmeyer-Massner, N. De Zanche, and K. P. Pruessmann, "Mechanically adjustable coil array for wrist MRI," *Magn. Reson. Med.*, vol. 61, no. 2, pp. 429–438, Feb. 2009.

[12] B. Wu *et al.*, "Flexible transceiver array for ultrahigh field human MR imaging," *Magn. Reson. Med.*, vol. 68, no. 4, pp. 1332–1338, Oct. 2012.

[13] R. Kriegl *et al.*, "Novel inductive decoupling technique for flexible transceiver arrays of monolithic transmission line resonators," *Magn. Reson. Med.*, vol. 73, no. 4, pp. 1669–1681, Apr. 2015.

[14] T. Zhang *et al.*, "A semiflexible 64-channel receive-only phased array for pediatric body MRI at 3T," *Magn. Reson. Med.*, vol. 76, no. 3, pp. 1015–1021, Sep. 2016.

[15] R. Frass-Kriegl *et al.*, "Flexible 23-channel coil array for high-resolution magnetic resonance imaging at 3 Tesla," *PLoS ONE*, vol. 13, no. 11, Nov. 2018, Art. no. e0206963.

[16] S. Hosseinnezhadian *et al.*, "A flexible 12-channel transceiver array of transmission line resonators for 7 T MRI," *J. Magn. Reson.*, vol. 296, pp. 47–59, Nov. 2018.

[17] J. R. Corea *et al.*, "Screen-printed flexible MRI receive coils," *Nature Commun.*, vol. 7, no. 1, Apr. 2016, Art. no. 10839.

[18] S. A. Winkler *et al.*, "Evaluation of a flexible 12-channel screen-printed pediatric MRI coil," *Radiology*, vol. 291, no. 1, pp. 180–185, 2019.

[19] J. A. Nordmeyer-Massner, N. De Zanche, and K. P. Pruessmann, "Stretchable coil arrays: Application to knee imaging under varying flexion angles," *Magn. Reson. Med.*, vol. 67, no. 3, pp. 872–879, Mar. 2012.

[20] A. Port *et al.*, "Towards wearable MR detection: A stretchable wrist array with on-body digitization," in *Proc. 26th Int. Soc. Magn. Reson. Med.*, Paris, France, 2018, p. 17.

[21] B. Gruber, R. Rehner, E. Laistler, and S. Zink, "Anatomically adaptive coils for MRI—A 6-Channel array for knee imaging at 1.5 Tesla," *Frontiers Phys.*, vol. 8, p. 80, Apr. 2020.

[22] A. Mehmann *et al.*, "On the bending and stretching of liquid metal receive coils for magnetic resonance imaging," *IEEE Trans. Biomed. Eng.*, vol. 66, no. 6, pp. 1542–1548, Jun. 2019.

[23] J. A. Malko, E. C. Mcclees, I. F. Braun, P. C. Davis, and J. C. Hoffman, "A flexible mercury-filled surface coil for MR imaging," *Amer. J. Neuroradiology*, vol. 7, no. 2, pp. 246–247, 1986.

[24] A. Port *et al.*, "Detector clothes for MRI: A wearable array receiver based on liquid metal in elastic tubes," *Sci. Rep.*, vol. 10, no. 1, p. 8844, Dec. 2020.

[25] A. Port, R. Luechinger, D. O. Brunner, and K. P. Pruessmann, "Conductive elastomer for wearable RF coils," in *Proc. 28th Int. Soc. Magn. Reson. Med.*, 2020, p. 1137.

[26] H. J. Zabel, R. Bader, J. Gehrig, and W. J. Lorenz, "High-quality MR imaging with flexible transmission line resonators.," *Radiology*, vol. 165, no. 3, pp. 857–859, Dec. 1987.

[27] N. Haziza, J. Bittoun, and S. Kan, "Multiturn split-conductor transmission-line resonator," *Rev. Sci. Instrum.*, vol. 68, no. 5, pp. 1995–1997, May 1997.

[28] T. Ruytenberg, A. Webb, and I. Zivkovic, "A flexible five-channel shielded-coaxial-cable (SCC) transceive neck coil for high-resolution carotid imaging at 7T," *Magn. Reson. Med.*, vol. 84, no. 3, pp. 1672–1677, Sep. 2020.

[29] M. S. M. Mollaei, C. C. Van Leeuwen, A. J. E. Raaijmakers, and C. R. Simovski, "Analysis of high impedance coils both in transmission and reception regimes," *IEEE Access*, vol. 8, pp. 129754–129762, 2020.

[30] K. Fujimoto *et al.*, "A tight-fit flexible high-impedance coil array for high-resolution imaging of small ex-vivo specimen using a human 7T scanner," in *Proc. 28th Int. Soc. Magn. Reson. Med.*, 2020, p. 4018.

[31] J.-C. Ginefri *et al.*, "Implanted, inductively-coupled, radiofrequency coils fabricated on flexible polymeric material: Application to *in vivo* rat brain MRI at 7T," *J. Magn. Reson.*, vol. 224, pp. 61–70, Nov. 2012.

[32] R. Frass-Kriegl *et al.*, "Multi-turn multi-gap transmission line resonators—Concept, design and first implementation at 4.7 T and 7 T," *J. Magn. Reson.*, vol. 273, pp. 65–72, Dec. 2016.

[33] X. Yang, T. Zheng, Y. Wu, and M. Finnerty, "Coaxial cable magnetic resonance image (MRI) coils," U.S. Patents 9 678 180 B2, Jun. 13, 2017.

[34] B. Zhang, D. K. Sodickson, and M. A. Cloos, "A high-impedance detector-array glove for magnetic resonance imaging of the hand," *Nature Biomed. Eng.*, vol. 2, no. 8, pp. 570–577, Aug. 2018.

[35] S. E. Zijlema, L. Van Dijk, J. J. W. Lagendijk, R. H. N. Tijssen, and C. A. T. Van Den Berg, "A radiolucent and flexible high impedance coil array to improve the imaging performance of a 1.5T MR-linac," in *Proc. 27th Int. Soc. Magn. Reson. Med.*, Montreal, QC, Canada, 2019, p. 1504.

[36] S.-I. Urayama, B. Zhang, K. Fujimoto, T. Okada, and M. A. Cloos, "A modular 7T highimpedance array for ex-vivo imaging," in *Proc. 27th Int. Soc. Magn. Reson. Med.*, Montreal, QC, Canada, 2019, p. 1541.

[37] R. S. Stormont *et al.*, "Systems for a radio frequency coil for MR imaging," U.S. Patents 20 190 277 926 A1, Sep. 12, 2019.

[38] T. Ruytenberg, A. Webb, and I. Zivkovic, "Shielded-coaxial-cable coils as receive and transceive array elements for 7T human MRI," *Magn. Reson. Med.*, vol. 83, no. 3, pp. 1135–1146, Mar. 2020.

[39] P. Gonord, S. Kan, and A. Leroy-Willig, "Parallel-plate split-conductor surface coil: Analysis and design," *Magn. Reson. Med.*, vol. 6, no. 3, pp. 353–358, Mar. 1988.

[40] P. Gonord, S. Kan, A. Leroy-Willig, and C. Wary, "Multigap parallel-plate bracelet resonator frequency determination and applications," *Rev. Sci. Instrum.*, vol. 65, no. 11, pp. 3363–3366, 1994.

[41] S. Serfaty, N. Haziza, L. Darrasse, and S. Kan, "Multi-turn split-conductor transmission-line resonators," *Magn. Reson. Med.*, vol. 38, no. 4, pp. 687–689, Oct. 1997.

[42] M. D. Harpen, "The theory of shielded loop resonators," *Magn. Reson. Med.*, vol. 32, no. 6, pp. 785–788, Dec. 1994.

[43] A. Stensgaard, "Optimized design of the shielded-loop resonator," *J. Magn. Reson., Ser. A*, vol. 122, no. 2, pp. 120–125, Oct. 1996.

[44] J. T. Vaughan, H. P. Hetherington, J. Otu, J. W. Pan, and G. M. Pohost, "High frequency volume coils for clinical NMR imaging and spectroscopy," *Magn. Reson. Med.*, vol. 32, no. 2, pp. 206–218, 1994.

[45] E. Laistler and E. Moser, "Handy magnetic resonance coils," *Nature Biomed. Eng.*, vol. 2, no. 8, pp. 557–558, Aug. 2018.

[46] P. K. H. Röschmann, "High-frequency coil system for a magnetic resonance imaging apparatus," U.S. Patents 4 746 866 A, May 24, 1988.

[47] J. Mispelter, M. Lupu, and A. Briguet, *NMR Probeheads for Biophysical and Biomedical Experiments: Theoretical Principles and Practical Guidelines*. London, U.K.: Imperial College Press, 2006.

[48] L. Darrasse and G. Kassab, "Quick measurement of NMR-coil sensitivity with a dual-loop probe," *Rev. Sci. Instrum.*, vol. 64, no. 7, pp. 1841–1844, Jul. 1993.

[49] S. Chung, D. Kim, E. Breton, and L. Axel, "Rapid B1+ mapping using a preconditioning RF pulse with TurboFLASH readout," *Magn. Reson. Med.*, vol. 64, no. 2, pp. 439–446, Aug. 2010.

[50] L. Darrasse, "Perspectives with cryogenic RF probes in biomedical MRI," *Biochimie*, vol. 85, no. 9, pp. 915–937, Sep. 2003.

[51] M. V. Vaidya, C. M. Collins, D. K. Sodickson, R. Brown, G. C. Wiggins, and R. Lattanzi, "Dependence of B1– and B1+ field patterns of surface coils on the electrical properties of the sample and the MR operating frequency," *Concepts Magn. Reson. B, Magn. Reson. Eng.*, vol. 46, no. 1, pp. 25–40, Feb. 2016.

[52] A. J. E. Raaijmakers, P. R. Luijten, and C. A. T. van den Berg, "Dipole antennas for ultrahigh-field body imaging: A comparison with loop coils," *NMR Biomed.*, vol. 29, no. 9, pp. 1122–1130, Sep. 2016.

[53] M. A. Ertürk, A. J. E. Raaijmakers, G. Adriany, K. Uğurbil, and G. J. Metzger, "A 16-channel combined loop-dipole transceiver array for 7 Tesla body MRI," *Magn. Reson. Med.*, vol. 77, no. 2, pp. 884–894, 2017.

[54] K. Lakshmanan, M. Cloos, R. Brown, R. Lattanzi, D. K. Sodickson, and G. C. Wiggins, "The 'loopole' antenna: A hybrid coil combining loop and electric dipole properties for Ultra-High-Field MRI," *Concepts Magn. Reson. B, Magn. Reson. Eng.*, vol. 2020, pp. 1–9, Sep. 2020.

[55] X. Yan, J. C. Gore, and W. A. Grissom, "Self-decoupled radiofrequency coils for magnetic resonance imaging," *Nature Commun.*, vol. 9, no. 1, p. 3481, Dec. 2018.

[56] B. Gruber, J. Stockmann, B. Guerin, and L. L. Wald, "Real-time image-based tracking of B0 shim elements in flexible matrix shim arrays for dynamic B0 shimming of the abdomen," in *Proc. 27th Int. Soc. Magn. Reson. Med.*, Montreal, QC, Canada, 2019, p. 1496.